33RD CONGRESS
OF THE INTERNATIONAL COUNCIL
OF THE AERONAUTICAL SCIENCES
STOCKHOLM, SWEDEN, 4-9 SEPTEMBER, 2022

ICAS 2022 SWEDEN

EFFECT OF LES LENGTH SCALE AND NUMERICAL SCHEME IN HYBRID RANS-LES OF FREE SHEAR LAYER FLOWS

Sebastian Arvidson[1,2], Magnus Carlsson[2] & Stefan Nilsson[1,2]

[1]Propulsion Systems, Saab Aeronautics, SE-581 88 Linköping, Sweden
[2]Division of Fluid Dynamics, Department of Mechanics and Maritime Sciences, Chalmers University of Technology, SE-412 96 Gothenburg, Sweden

Abstract

The effect of LES length scales, treatment of near-wall functions in the LES domain and numerical discretization schemes has been evaluated in SA-DDES simulations of free shear layer flows. In a fundamental low Mach number free shear layer flow it has been shown that the choice of LES length scale, how the near-wall functions are treated in LES mode and the numerical scheme is of vital importance for an accurate prediction of the mixing and the resolved turbulent Reynolds stresses. In simulations of a transonic flow over the generic M219 cavity it was observed that the choice of LES length scale is not as evident as in the fundamental free shear layer. However, it was clear that vorticity based LES length scales improve the prediction of the overall sound pressure levels, the Rossiter modes and the mean flow field compared to Δ_{max} used in the original formulation of SA-DDES.

Keywords: Free shear layer flows, Turbulence-resolving simulations, Hybrid RANS-LES, Grey-area mitigation, LES length scale

1. Introduction

Since Spalart et al. [1] presented the Detached-Eddy Simulation (DES) concept in 1997, much research efforts have been put into improvements and verification of different hybrid RANS-LES concepts. Improved variant of DES have been proposed such as Delayed DES (DDES)[2] and Improved DDES (IDDES) [3]. Hybrid RANS-LES models can generally be split in two categories: zonal and non-zonal methods. In zonal methods RANS and LES regions are prescribed by the user whereas in non-zonal methods the model itself decide if the flow should be modeled in RANS mode or in LES mode. The DES concept was originally a non-zonal method. However, zonal approaches based on DES and DDES has been developed during the years, see e.g [4, 5, 6].

The idea with the DDES approach was to ensure that the model safely models attached boundary layers in RANS mode whereas flow separations as well as the off-wall regions are modeled with LES. Compared to DES, where the switch between RANS and LES is strictly dependent on the local grid resolution and the turbulent RANS length scale, the DDES approach involves a boundary layer shielding function which detects whether the boundary layer is attached or not and from that determine if the RANS or LES mode should be used.

Thus, the DDES model is an attractive approach for industrial applications since it often is hard to fully control the grid resolution needed for zonal methods or the DES model from 1997, in order to fully cover attached boundary layers in RANS mode. It is, however, well known that the original formulation of the DDES model suffers from a slow transition from modeled turbulent stresses in RANS mode to resolved turbulent stresses in LES mode, i.e. the so-called grey area (e.g. [7]).

The turbulence-resolving capability in LES mode of DES and hybrid RANS-LES approaches is much dependent on the choice of the LES length scale. In free shear layer flows the choice of LES length scale is vital in order to reduce the grey area and achieve a rapid transition from RANS modeled turbulent stresses to well established LES resolved turbulent stresses [8, 9]. Hence, a DDES framework

with a considerably reduced grey area would be of high priority for industrial aeronautical applications. In this paper we therefore investigate the effect of different LES length scales in combination with the SA-DDES model [2]. Moreover, we investigate the effect of the numerical scheme on the turbulence-resolving capability in LES mode and how the near-wall functions in the SA model should be treated in LES mode of SA-DDES.
The paper is arranged as follows. The turbulence modeling approach is introduced which is followed by a presentation of the numerical method used in the flow simulations. The results for decaying homogeneous isotropic turbulence, a fundamental free shear layer flow and the transonic flow over the generic M219 cavity are presented and discussed. Finally, the paper is summarized and conclusions are presented.

2. Turbulence modeling

In this work we use the DDES approach [2] based on the Spalart-Allmaras (SA) RANS model [10]. The DDES length scale reads

$$l_{DDES} = l_{RANS} - f_d \max\left(0, l_{RANS} - l_{LES}\right) \tag{1}$$

where $l_{RANS} = d$, is the SA RANS length scale and f_d is the so-called shielding function, which should prevent LES content from penetrate into the RANS modeled boundary layer, see Eq. 2.

$$f_d = 1 - \tanh\left(\left[C_1 r_d\right]^{C_2}\right) \tag{2}$$

where $C_1 = 8$ and $C_2 = 3$. The function r_d reads

$$r_d = \frac{\nu_t + \nu}{\sqrt{U_{i,j}U_{i,j}}\kappa^2 d^2} \tag{3}$$

where ν_t is the kinematic turbulent viscosity, ν the molecular viscosity $U_{i,j}$ the velocity gradients, κ the von Karman constant and d the distance to the closest wall. The f_d-function is 0 in RANS mode and 1 in LES mode. The LES length scale reads

$$l_{les} = \Psi C_{DES} \Delta \tag{4}$$

where $C_{DES} = 0.65$ is the DES constant and Δ is the local filter width. The function Ψ that was proposed by Spalart et al. [2], and has been further explored by e.g. Shur et al. [3], Mockett [11] and Arvidson et al. [12] in DES variants and with various underlying RANS models, is a correction function which aims to neutralize the effect of near-wall functions (NWF) in LES mode.
The near-wall functions are designed in order to achieve a correct asymptotic behaviour of the RANS modeled turbulence in the near-wall region. The near-wall functions are activated at low local turbulent Reynolds numbers. Hence, in LES mode of e.g. DES/DDES/IDDES, where only the turbulent subgrid scales are modeled, the local turbulent Reynolds number can be low enough to activate the near-wall functions, which might harm a physically correct decay of the resolved turbulence. The impact of activated near-wall functions on a turbulence-resolving LES flow is however not fully understood and has to be further investigated.
The Ψ-function is derived based on the assumption that the turbulent viscosity can be expressed on a generalized Smagorinsky form when the turbulence is in local equilibrium, i.e. when the convection and diffusion terms in the transport equation/equations of the RANS model are negligible and the production term is equal to the destruction term. The correction function Ψ for the SA model (without involving the tripping terms) reads

$$\Psi = \sqrt{\min\left[10^2, \frac{1 - \frac{c_{b1}}{c_{w1}\kappa^2 f_w^*} f_{v2}}{f_{v1}}\right]} \tag{5}$$

For further details the reader is referred to the original papers for the SA model [10] and the DDES concept [2].

With inclusion of the Ψ-function in the LES length scale, l_{LES}, it is possible to formulate a non-zonal RANS-LES approach with regards to the near-wall functions. An alternative way to the introduction of the Ψ-function in the LES length scale is to deactivate the near-wall functions in LES mode. In the context of a SA based hybrid RANS-LES approach it means that one set $f_{v1}=1,\ f_{v2}=0$ and $f_w=1$ in LES mode, see e.g. [4, 5, 6]. In this work we evaluate the effect of activation/deactivation of the correction function Ψ and the near-wall functions in LES mode of SA-DDES by comparing the following three approaches

1. Near-wall functions are activated, Ψ is activated
2. Near-wall functions are activated, Ψ is deactivated ($\Psi=1$)
3. Near-wall functions are deactivated ($f_{v1}=1,\ f_{v2}=0,\ f_w=1$), Ψ is deactivated ($\Psi=1$)

We use the f_d-function to deactivate the near-wall functions. For $f_d \geq f_{d0}$, where $f_{d0}=0.95$, the near-wall functions are deactivated in Approach 3.
In addition to Δ_{max}, see Eq. (6), which is used in the original formulation of the DDES model, we use $\widetilde{\Delta}_\omega$ [13, 9] and Δ_{SLA} (SLA - Shear Layer Adaptive) [9], which both adapts its filter width in free shear layer flows with the aim to avoid an excess of turbulent subgrid scale (SGS) viscosity.

$$\Delta_{max} = \max\left(\Delta_x, \Delta_y, \Delta_z\right) \tag{6}$$

Equation (6) represents the maximum edge length of the local control volume. In computational grids adapted for free shear layer simulations the cells are often highly anisotropic. In such grids Δ_{max} is commonly set by the spanwise grid resolution which often gives an excess of turbulent SGS viscosity. The length scale $\widetilde{\Delta}_\omega$, however, is able to adapt its width based on the local vorticity direction in the flow. For a hexahedral cell $\widetilde{\Delta}_\omega$ is formulated as in Eq. (7).

$$\widetilde{\Delta}_\omega = \frac{1}{\sqrt{3}} \max_{n,m=1,8} \mid (l_n - l_m) \mid,\ l_n = n_\omega \times (r_n - r),\ n_\omega = \frac{\omega}{\|\omega\|} \tag{7}$$

Here $l_n = n_\omega \times r_n$ where n_ω is the unit vector aligned with the vorticity vector. The length scale $\widetilde{\Delta}_\omega$ should be interpreted as the maximum diameter of points generated by the cross product l_n divided by $\sqrt{3}$. The division of $\sqrt{3}$ is made to approximately recover Δ_{max} on cubic cells. It should, however, be noted that this factor is dependent on the cell type in order to recover Δ_{max}.
To further force the reduction of the turbulent SGS viscosity in free shear layers, the F_{KH} function was proposed by Shur et al. [9] to be added to $\widetilde{\Delta}_\omega$ to give Δ_{SLA} as in Eq. (8). The F_{KH} function is based on a vortex tilting measure (VTM) with the aim to detect Kelvin-Helmholtz like structures and rapidly reduce the LES filter width in these regions. The vortex tilting measure $\langle VTM \rangle$ is in our implementation a volume average of the neighbouring cells.

$$\Delta_{SLA} = \widetilde{\Delta}_\omega F_{KH}\left(\langle VTM \rangle\right) \tag{8}$$

The function F_{KH} takes values between zero and one, where one is its natural value and a reduction towards zero takes place in flows where Kelvin-Helmholtz like structures are detected. By achieving this further reduction of the turbulent SGS viscosity compared to $\widetilde{\Delta}_\omega$, the aim is to break up the two dimensional Kelvin-Helmholtz structures and form physical three-dimensional turbulent structures. The vortex titling meassure and F_{KH} is given in Eqs. (9)-(10).

$$VTM \equiv \frac{\sqrt{6} \mid \left(\hat{S} \cdot \omega\right) \times \omega \mid}{\omega^2 \sqrt{3tr\left(\hat{S}^2\right) - \left[tr\left(\hat{S}\right)\right]^2}} \max\{1, (0.2\nu/\nu_t)\} \tag{9}$$

$$F_{KH}\left(\langle VTM \rangle\right) = \max\{F_{KH}^{\min}, \min\{F_{KH}^{\max}, F_{KH}^{\min} + \frac{F_{KH}^{\max} - F_{KH}^{\min}}{a_2 - a_1}\left(\langle VTM \rangle - a_1\right)\}\} \tag{10}$$

where $F_{KH}^{\max} = 1.0$ and $F_{KH}^{\min}$, a_1 and a_2 are adjustable empirical parameters which are set to 0.1, 0.15 and 0.3, respectively.

There is an interaction between the shielding of the boundary layer given by the f_d-function and the turbulent SGS viscosity given by the LES length scale Δ. Both $\widetilde{\Delta}_\omega$ and Δ_{SLA} aim at reducing the local SGS viscosity. Hence, by setting Δ to $\widetilde{\Delta}_\omega$ or Δ_{SLA} in Eq. (4), will lead to a degraded shielding of the boundary layer, which will not be treated safely in RANS mode due to the reduced local turbulent viscosity (see Eqs. 2-3). With the aim to avoid LES content to penetrate into the boundary layer, $\widetilde{\Delta}_\omega$ and Δ_{SLA} are only applied to the DDES length scale when the shielding function $f_d \geq f_{d0}$, elsewhere Δ_{max} is used.

3. Numerical method

All simulations in this paper have been performed using the unstructured edge- and node-based compressible Navier-Stokes solver M-Edge [14, 15]. The solver is applicable for both structured and unstructured grids. The Navier-Stokes equations are discretized with a finite-volume approximation and are integrated in time using a 2nd-order backward differencing scheme, together with a dual-time stepping methodology which uses a fully implicit steady-state time marching scheme [16]. The boundary conditions are based on a weak formulation [17].

The viscous fluxes are discretized using a 2nd-order central differencing scheme. The effect of different discretization schemes for the inviscid fluxes are evaluated. The low-dissipation and low-dispersion (LD2) scheme by Löwe et al. [18] is used as reference. For comparison we exclude the low-dispersion part so that only the low-dissipative matrix dissipation (MD) scheme is used. Furthermore, we also apply a scalar dissipation (SD) scheme [19] for comparison. Low Mach number preconditioning (LMP) based on Langer [20] has been used in test cases for decaying homogeneous isotropic turbulence and the fundamental free shear layer. For further details on how the numerical scheme is implemented in M-Edge, the reader is referred to Carlsson et al. [21]. Numerical schemes, LES length scales, if low Mach number preconditioning (LMP) has been used or not and which approach that has applied for the treatment of the near-wall function in the LES region are summarized for the different test cases in Table 1.

Table 1 – Summary of numerical schemes and simulation approaches.

Test case	Scheme	LMP	NWF/Ψ	Δ
DHIT	LD2	Yes	1, 2, 3	Δ_{max}, $\widetilde{\Delta}_\omega$, Δ_{SLA}
DHIT	MD	Yes	3	Δ_{SLA}
DHIT	SD	Yes	3	Δ_{SLA}
Free shear layer	LD2	Yes	1, 2, 3	Δ_{max}, $\widetilde{\Delta}_\omega$, Δ_{SLA}
Free shear layer	MD	Yes	3	Δ_{SLA}
Free shear layer	SD	Yes	3	Δ_{SLA}
Cavity	LD2	No	3	Δ_{max}, $\widetilde{\Delta}_\omega$, Δ_{SLA}
Cavity	MD	No	3	Δ_{SLA}
Cavity	SD	No	3	Δ_{SLA}

4. Results and discussion

Assessment of the LES length scales given by Eqs. (6)-(8), numerical schemes as well as the effect of the correction function Ψ and its interaction with the near-wall functions in LES mode is evaluated for Decaying Homogeneous Isotropic Turbulence (DHIT), a free shear layer flow and in transonic flow over the generic M219 cavity.

4.1 Decaying Homogeneous Isotropic Turbulence

Decaying Homogeneous Isotropic Turbulence (DHIT) have been simulated using a domain size of $(2\pi)^3$. The computational domain is discretized with cubic cells. Simulations on three grid resolutions have been performed; $\mathbf{N} = 32^3$, 64^3 and 128^3. Periodic boundary conditions have been applied in x, y and z directions. An initial velocity field have been generated by the widely used computer

program from Professor Strelets' group in St. Petersburg. Energy spectra are presented at two non-dimensional times: $\widetilde{t} = 0.87$ and 2.0. Experimental data by Comte-Bellot and Corrsin [22] is used as reference. The SA-DDES model has been forced to work in LES mode.
Turbulent energy spectra and decay of turbulent kinetic energy for the three LES length scales and the different discretization schemes are given in Figure 1. In these simulations Ψ and near-wall functions are deactivated. Data for the different length scales coincides on all three grids since they recover the same filter width on cubic cells. The effect of discretization scheme is small. Differences are observed at higher wave numbers, where the higher accuracy of the LD2 scheme compared to the other two schemes are favorable.

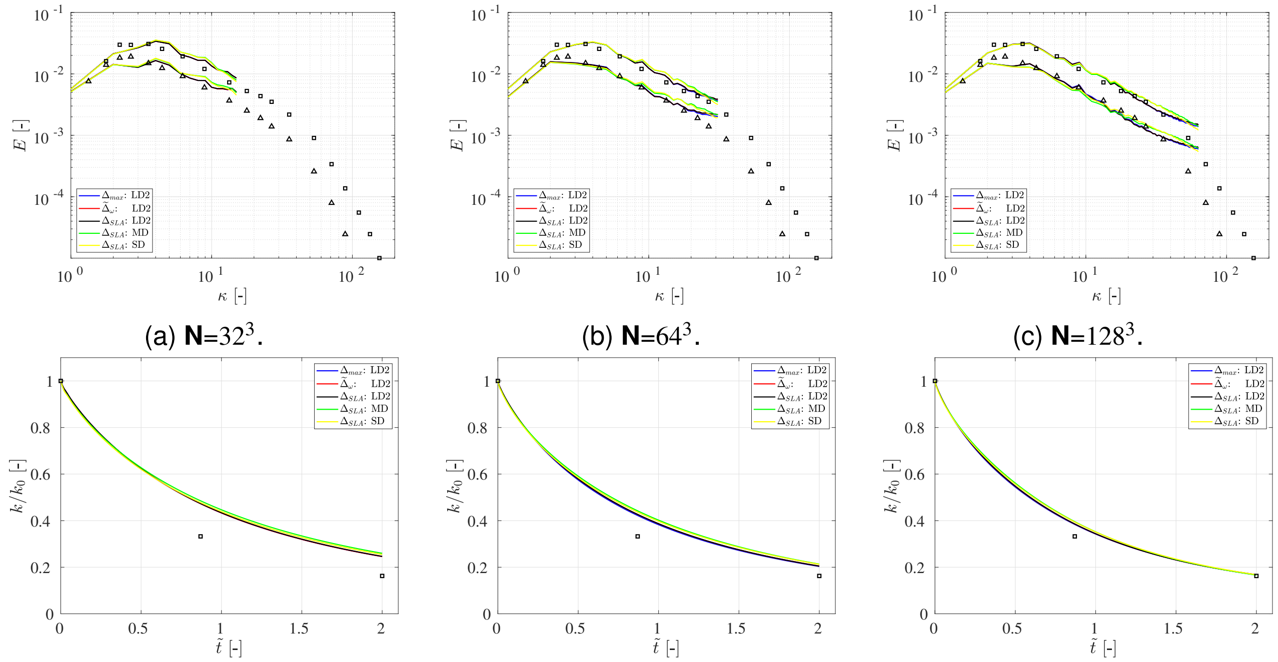

(a) **N**=32^3. (b) **N**=64^3. (c) **N**=128^3.

(d) **N**=32^3. (e) **N**=64^3. (f) **N**=128^3.

Figure 1 – DHIT. SA-DDES in LES mode. Near-wall function deactivated ($f_{v1} = 1$, $f_{v2} = 0$, $f_w = 1$) and $\Psi = 1$. Effect of LES length scale and numerical scheme. (a)-(c) Energy spectra at two non-dimensional times $\tilde{t} = 0.87$ ($\Box$) and 2.0 ($\triangle$). (d)-(f) Decay of turbulent kinetic energy.

Results from simulations where different approaches for how the near-wall functions and the correction function Ψ are treated are presented in Figure 2. In these simulations $\Delta = \Delta_{SLA}$. On grid **N**=32^3 and **N**=64^3, an almost negligible difference is recognized between approach 1 and 2. On the finest grid, **N**=128^3, approach 2 deviates from approach 1, indicating that the local turbulent Reynolds numbers are low enough to activate the near-wall functions and give too low a dissipation for higher wave numbers. With approach 3 (NWR and Ψ deactivated) the decay of turbulence is underpredicted for the highest wave numbers. Approach 1 (NWR and Ψ activated) gives the best results compared to the experimental data and it seems that the SA model needs the near-wall functions together with Ψ in order to give consistent results in DHIT.

4.2 Free shear layer flow

The free shear layer flow, investigated experimentally by Delville [23], has been simulated with the computational setup shown in Figure 3. The computational domain includes an infinitely thin flat plate, with boundary layers on each side, and the region downstream of the flat plate trailing edge where the two boundary layers mix. The boundary layers on each side of the flat plate have different freestream velocities and different Reynolds numbers. The experimental boundary layer properties at the trailing edge are presented in Table 2.
The focus region of the grid, i.e. the region from the flat plate trailing edge at $x = 0$ m to $x = L_{ref} = 1$ m, consists of $(n_x, n_y, n_z) = (640, 96, 192)$ cells. The total number of hexahedral grid cells are 13.7 million. Total states inlet boundary conditions as well as a static pressure outlet boundary condition

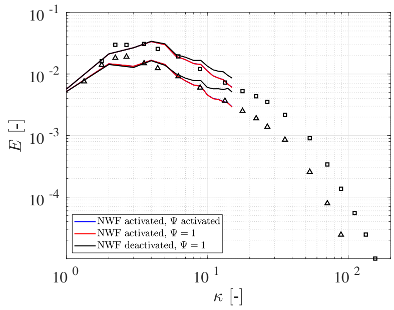

(a) **N**=32^3.

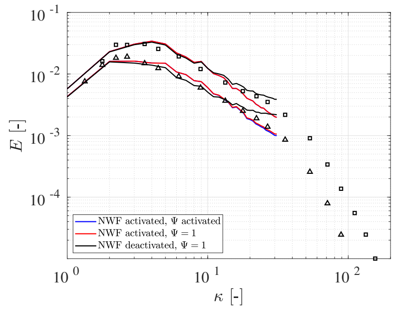

(b) **N**=64^3.

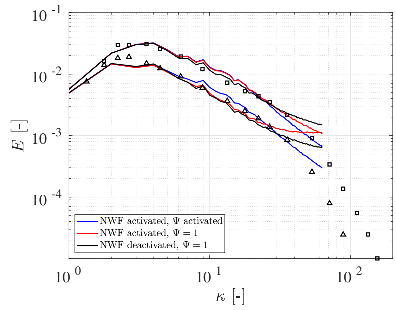

(c) **N**=128^3.

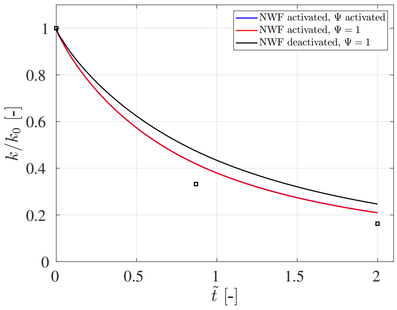

(d) **N**=32^3.

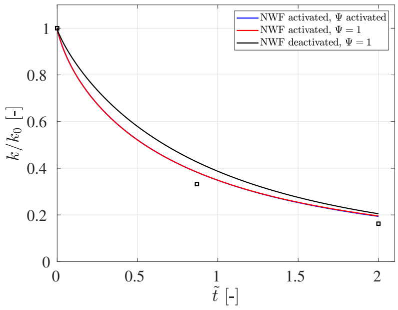

(e) **N**=64^3.

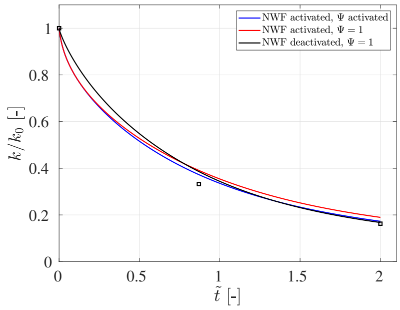

(f) **N**=128^3.

Figure 2 – DHIT. SA-DDES in LES mode using $\Delta = \Delta_{SLA}$. Effect of near-wall functions (NWF) and Ψ-function. (a)-(c) Energy spectra at two non-dimensional times $\tilde{t} = 0.87$ ($\square$) and 2.0 ($\triangle$). (d)-(f) Decay of turbulent kinetic energy.

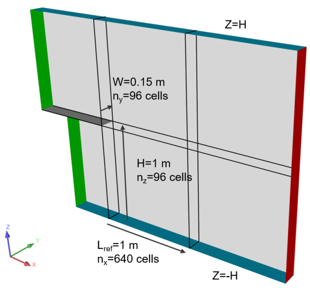

(a) Computational domain.

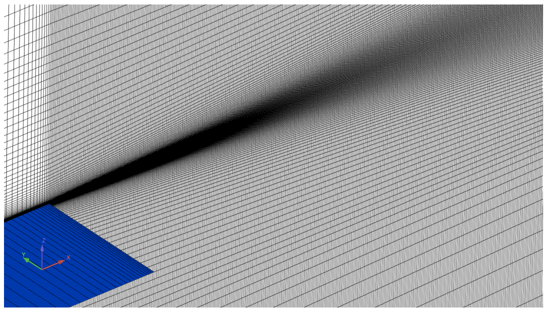

(b) Computational grid.

Figure 3 – Free shear layer flow. (a) Computational domain. Green boundaries are inlets and red boundary is outlet. (b) Computational grid. Blue boundary is the trailing edge part of the flat plate and the white boundary is one of the two periodic boundaries.

Table 2 – Flow conditions of the boundary layers at $x = -10$ mm. Data from experiment [23].

Measure	Notation	High velocity BL	Low velocity BL
Velocity	U_∞	41.54 m/s	22.40 m/s
Thickness	δ	9.6 mm	6.3 mm
Displacement thickness	δ_1	1.4 mm	1.0 mm
Momentum thickness	θ	1.0 mm	0.73 mm
Shape factor	H	1.35	1.37
Re-number based on θ	Re_θ	2900	1200
Turbulence level	u'/U_∞	$\sim 0.3\%$	$\sim 0.3\%$

have been applied to match the velocities given in Table 2. Periodic boundaries have been used in the spanwise direction and symmetry boundary conditions have been applied at $z = H$ and $z = -H$. A time step of $\Delta t = 2.5 \cdot 10^{-5}$ s have been used. Time-averaging and statistical data are based on 0.5

seconds. To establish the flow field 0.25 seconds were simulated. In total 0.75 seconds have been simulated. For this test case $<\cdot>$ means averaging in time and in the spanwise y-direction.
To evaluate the free shear layer growth, vorticity thickness and momentum thickness are used. Since this test case can be considered to be incompressible the vorticity and momentum thickness are defined as follows

$$\delta_\omega = \frac{U_a - U_b}{(\partial U/\partial y)_{y=0}} \tag{11}$$

$$\theta = \int_{-\infty}^{\infty} \frac{U - U_b}{U_a - U_b}\left(1 - \frac{U - U_b}{U_a - U_b}\right) dy \tag{12}$$

where, U_a and U_b are taken as the streamwise velocity at $z = -H$ and $z = H$, respectively.

4.2.1 Effect of near-wall functions and Ψ

The approach used to treat the near-wall functions and Ψ has a large impact on the turbulent viscosity downstream of the flat plate trailing edge. As a secondary effect, the mixing of the free shear layer is affected. Results for the three approaches to treat the near-wall functions and Ψ as well as the three LES length scales are summarized in Figures 4-6.

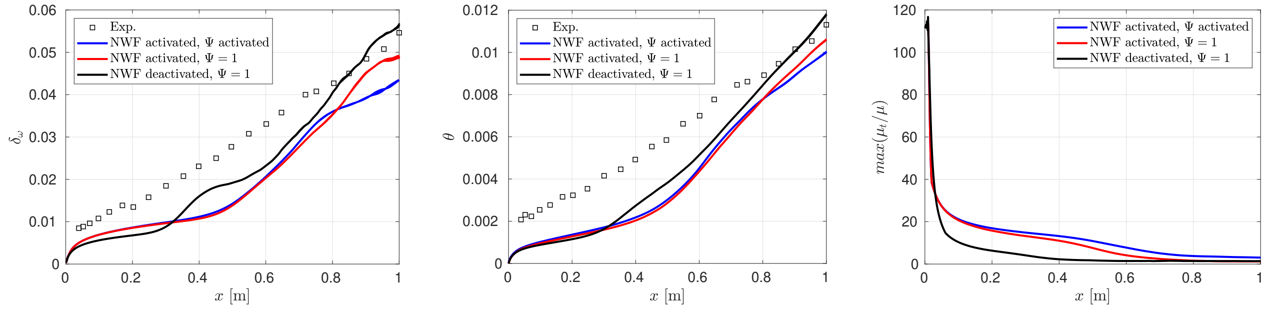

(a) Vorticity thickness. (b) Momentum thickness. (c) Turbulent viscosity.

Figure 4 – Free shear layer flow. Effect of near-wall functions (NWF) and Ψ-function, $\Delta = \Delta_{max}$.

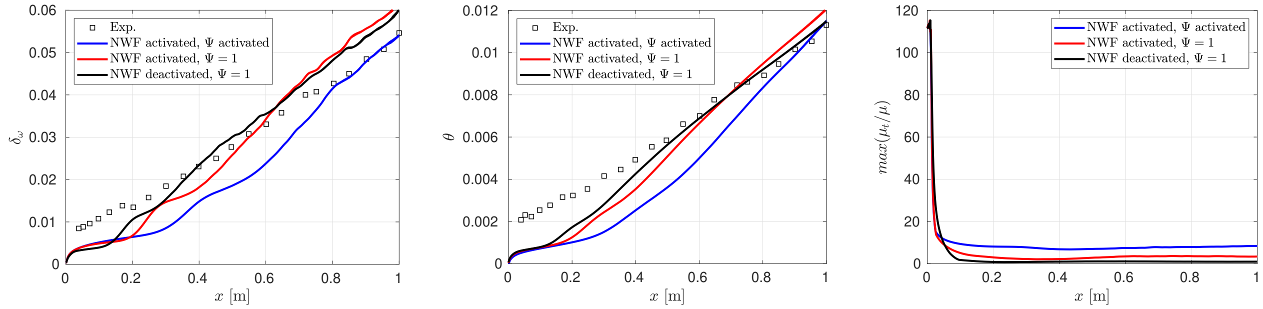

(a) Vorticity thickness. (b) Momentum thickness. (c) Turbulent viscosity.

Figure 5 – Free shear layer flow. Effect of near-wall functions (NWF) and Ψ-function, $\Delta = \widetilde{\Delta}_\omega$.

For all three LES length scales, approach 1 (NWF and Ψ activated) gives the highest level of turbulent viscosity and the most delayed mixing of the free shear layer. Approach 3 is to be the most promising approach to mitigate the grey area while approach 2 performs in between approach 1 and 3.
Both $\widetilde{\Delta}_\omega$ and Δ_{SLA} are designed to minimize its filter width when free shear layer flows are detected to reduce the turbulent viscosity and thus promote the development of resolved turbulence. With low levels of turbulent viscosity, i.e. small turbulent Reynolds numbers, the near-wall functions and the Ψ-function will be activated. In the DHIT simulations presented in Figure 2, the Ψ-function successfully neutralizes the effect from the near-wall functions and the decay of turbulence aligns with the experimental data for all grid resolutions evaluated.

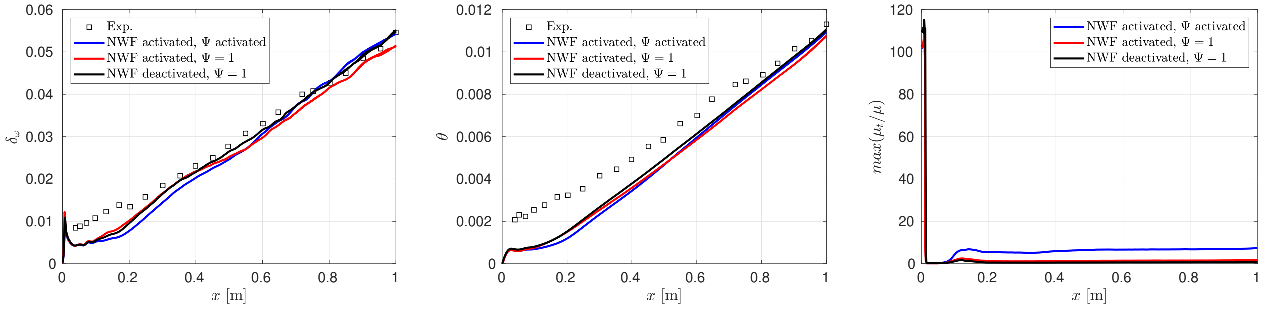

(a) Vorticity thickness. (b) Momentum thickness. (c) Turbulent viscosity, $\Delta = \Delta_{SLA}$.

Figure 6 – Free shear layer flow. Effect of near-wall functions (NWF) and Ψ-function, $\Delta = \Delta_{SLA}$.

A rapid reduction of the turbulent viscosity is successfully achieved shortly downstream of the trailing edge of the flat plate with both $\widetilde{\Delta}_\omega$ and Δ_{SLA} as seen in Figure 5 (c) and 6 (c). With $\widetilde{\Delta}_\omega$ and approach 1, the Ψ-function limits the reduction to $\mu_t/\mu = 10$. With Δ_{SLA} a further reduction is observed shortly downstream of the trailing edge, but a sudden increase in the turbulent viscosity is observed at $x = 0.1$ m to the same level as for $\widetilde{\Delta}_\omega$. This behavior of the turbulent viscosity indicates that the Ψ-function strongly affects the turbulent viscosity and that Ψ reaches its maximum value of 10 (see Eq. 5) in this region.
The F_{KH}-function included in Δ_{SLA} has a more direct effect on the turbulent viscosity than the Ψ-function. When Kelvin-Helmholz like structures are detected F_{KH} turns to zero. Hence, the destruction term in the SA transport equation gets very large quickly and the turbulent viscosity is in turn rapidly reduced. Even though the Ψ-function reaches its maximum value in this region, F_{KH} will always limit μ_t as long as it is close to zero which it is for $x < 0.1$ m. Downstream of $x = 0.1$ m the two dimensional turbulent structures have started to break-up which makes F_{KH} larger and the effect of Ψ as the lower limiter for the turbulent viscosity is seen.
The effect of Ψ on the turbulent viscosity for Δ_{max} is even larger than for $\widetilde{\Delta}_\omega$ and Δ_{SLA}. However, Δ_{max} itself produces higher levels of turbulent subgrid scale viscosity than the other LES length scales, which gives too much of a delay in the formation of resolved turbulence and thus an overall poor prediction of the shear layer mixing.
From hereon approach 3, i.e. near-wall functions and Ψ are deactivated in the LES mode of SA-DDES, is applied in the simulations of the free shear layer and the transonic flow over the generic M219 cavity.

4.2.2 Effect of LES length scale

The streamwise velocity profiles of the free shear layer are given in Figure 7. The boundary layer on the flat plate is modeled in RANS mode with the SA-DDES model and the achieved velocity profiles agrees well with experimental data as seen in Figure 7 (a). Further downstream in the free shear layer at $x = 200$ mm there is a clear discrepancy between the simulations and the experimental data, especially on the low speed side of the shear layer. This is due to the grey area problem, i.e. there is a too slow development of resolved turbulence in the LES region, which gives an underpredicted mixing of the two boundary layers. At $x = 650$ mm, the simulations using $\widetilde{\Delta}_\omega$ and Δ_{SLA} almost recover the experimental data with only a small discrepancy left for Δ_{max}. At $x = 800$ mm all three velocity profiles almost coincide with each other.
The effect on the velocity profiles using the different LES length scales are well summarized by the vorticity thickness and the momentum thickness, which are given in Figure 8. The Δ_{SLA} length scale captures both the growth of the vorticity and the momentum thickness reasonably well. With the standard LES length scale used in SA-DDES, Δ_{max}, there is a strong delay in the mixing of the two boundary layers as seen to some extent also in the velocity profiles, giving a too slow growth of both the vorticity and the momentum thickness. With $\widetilde{\Delta}_\omega$ a slight delay is recognized compare to Δ_{SLA} close to the flat plate trailing edge but with a slight overprediction further downstream.
There is a big difference close to the flat plate trailing edge in the turbulent viscosity levels between the different LES length scales as shown in Figure 8 (c). With Δ_{SLA}, the F_{KH} function is activated as

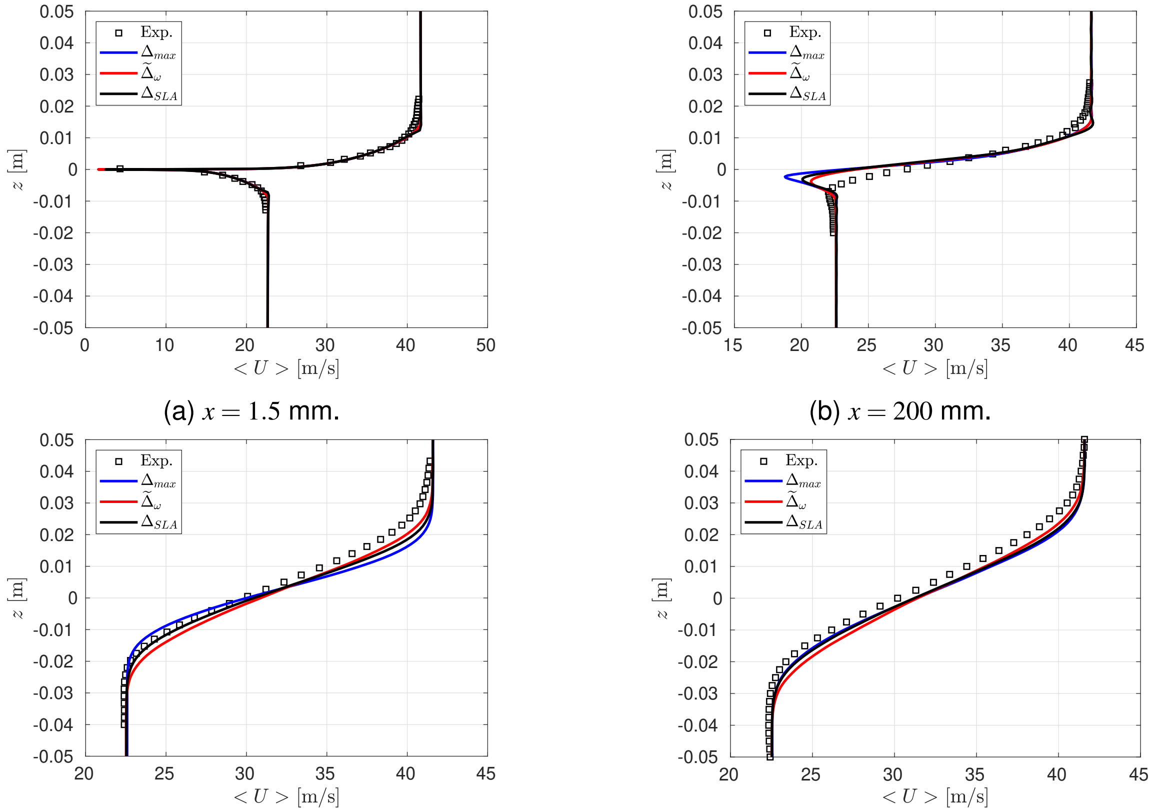

(a) $x = 1.5$ mm. (b) $x = 200$ mm.

(c) $x = 650$ mm. (d) $x = 800$ mm.

Figure 7 – Free shear layer flow. Streamwise velocity, $< U >$.

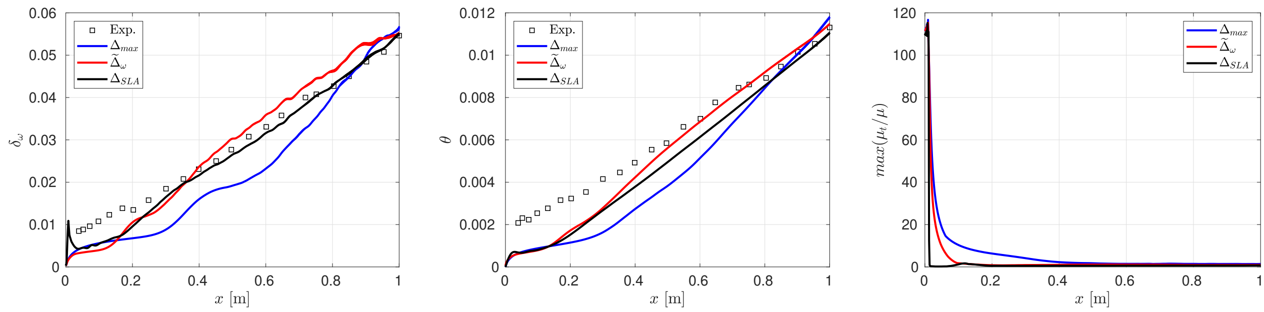

(a) Vorticity thickness. (b) Momentum thickness. (c) Turbulent viscosity, $\Delta = \Delta_{SLA}$.

Figure 8 – Free shear layer flow. Shear layer growth and turbulent viscosity.

it should in the early stage of the free shear layer and the turbulent viscosity reduces to almost zero. With Δ_{max} and $\widetilde{\Delta}_\omega$, the turbulent viscosity is larger in the early stage of the free shear layer. However, with $\widetilde{\Delta}_\omega$ the turbulent viscosity reduces to the same level as for Δ_{SLA} for $x > 0.1$ m. The larger turbulent viscosity given with Δ_{max} is strongly reflected in the turbulence-resolving capability and the mixing of the two boundary layers as shown in Figures 9-12.

With Δ_{max} the resolved stresses at $x = 200$ mm are almost negligible, which highlights the grey area given with this LES length scale in combination with the SA-DDES model. The resolved stresses are in overall reasonably well predicted with both $\widetilde{\Delta}_\omega$ and Δ_{SLA}. Both length scales underpredicts the thickness of the shear layer at $x = 200$ mm. Peak values for all resolved stresses are very well captured with Δ_{SLA}. The vertical normal stress is overpredicted with $\widetilde{\Delta}_\omega$ at $x = 200$ mm. Further downstream at $x = 650$ and 800 mm a slight overprediction of the resolved turbulent stresses are observed for both $\widetilde{\Delta}_\omega$ and Δ_{SLA}, especially in the vertical direction at $x = 650$ and 800 mm. The resolved shear stresses are similar between $\widetilde{\Delta}_\omega$ and Δ_{SLA} with a good agreement to the experimental data. As a consequence of the low levels of resolved turbulent stresses in the early stage of the free

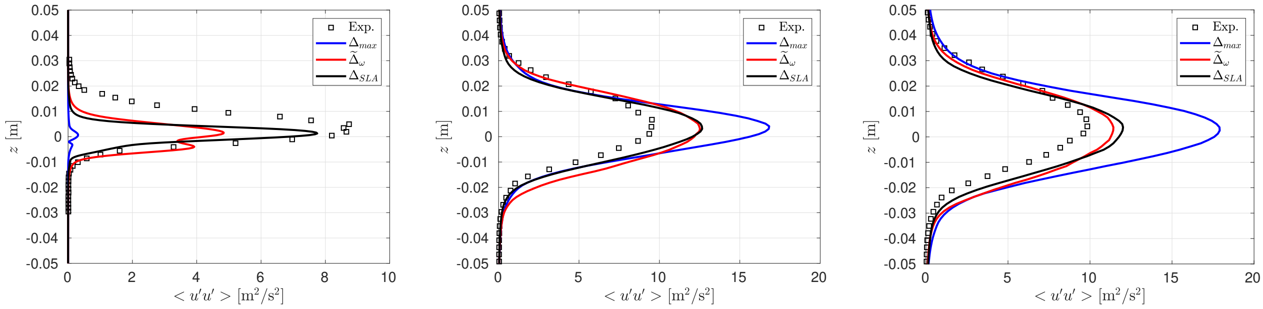

(a) $x = 200$ mm. (b) $x = 650$ mm. (c) $x = 800$ mm.

Figure 9 – Free shear layer flow. Resolved streamwise normal stress, $< u'u' >$.

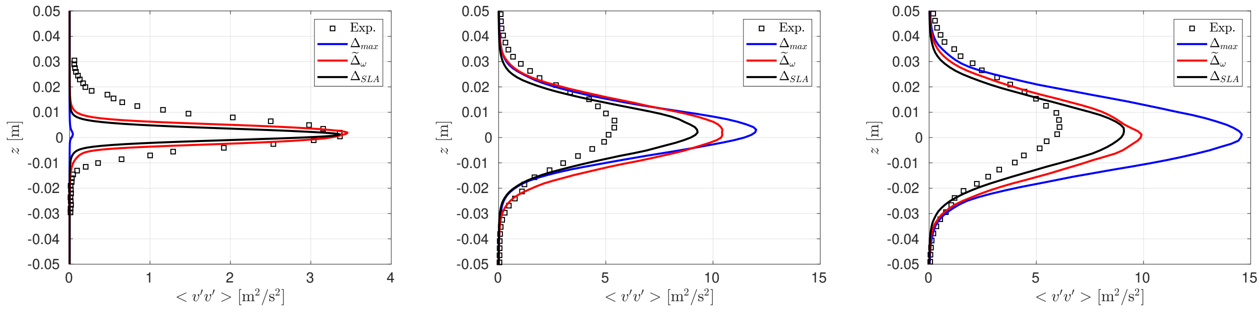

(a) $x = 200$ mm. (b) $x = 650$ mm. (c) $x = 800$ mm.

Figure 10 – Free shear layer flow. Resolved spanwise normal stress, $< v'v' >$.

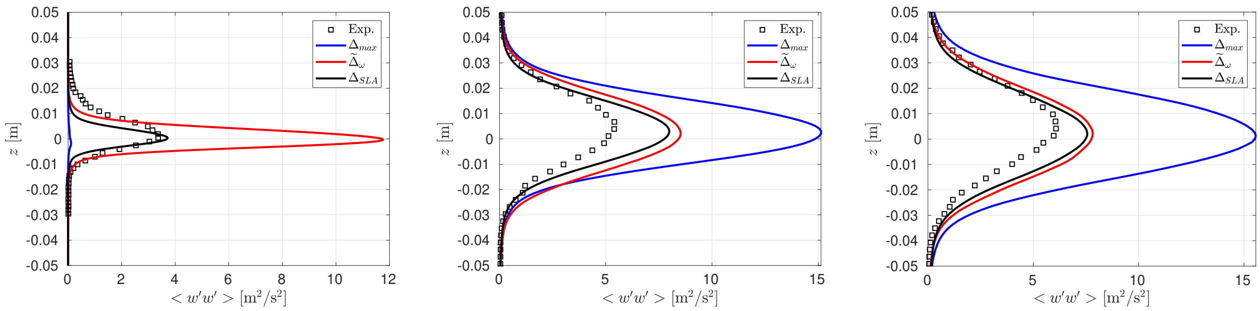

(a) $x = 200$ mm. (b) $x = 650$ mm. (c) $x = 800$ mm.

Figure 11 – Free shear layer flow. Resolved vertical normal stress, $< w'w' >$.

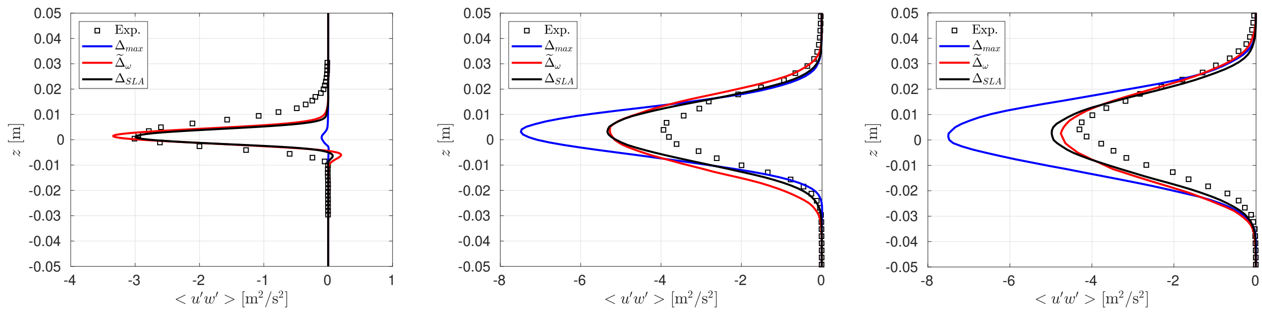

(a) $x = 200$ mm. (b) $x = 650$ mm. (c) $x = 800$ mm.

Figure 12 – Free shear layer flow. Resolved shear stress, $< u'w' >$.

shear layer for Δ_{max}, the resolved stresses at $x = 650$ mm and 800 mm are greatly overpredicted due to too large unphysical turbulent structures.

In Figure 13 resolved turbulent structures are visualized using iso-surfaces of Q-criterion. The large grey area given with Δ_{max} is clearly seen since there is a large part of the shear layer which does not show any appearance of resolved turbulent structures. With $\widetilde{\Delta}_{\omega}$ and Δ_{SLA}, only a short region downstream of the flat plate trailing edge consists of two-dimensional Kelvin-Helmholtz structures which rapidly breaks up into three-dimensional structures. However, structures are somewhat finer with Δ_{SLA} compared to $\widetilde{\Delta}_{\omega}$ close to the trailing edge which may explain the overprediction of the resolved vertical Reynolds stress at $x = 200$ mm with $\widetilde{\Delta}_{\omega}$.

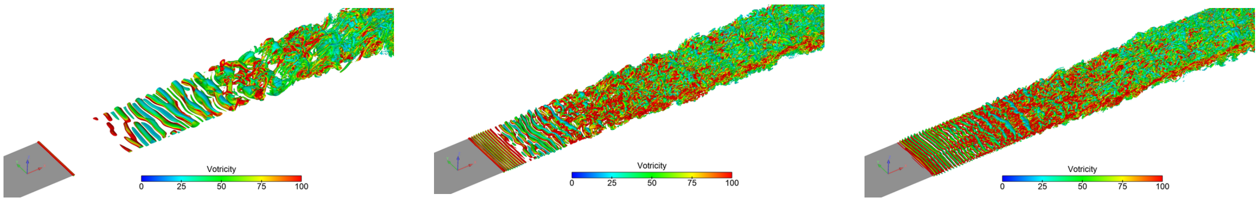

(a) $\Delta = \Delta_{max}$. (b) $\Delta = \widetilde{\Delta}_{\omega}$. (c) $\Delta = \Delta_{SLA}$.

Figure 13 – Free shear layer flow. Resolved turbulent structures visulized using iso-surfaces of Q-criterion $Q\left(L_{ref}/U_{low}\right)^2 = 100$. Colorbar shows scaled vorticity magnitude $\parallel \omega \parallel \left(L_{ref}/U_{low}\right)$.

4.2.3 Effect of numerical scheme

In these simulations Δ_{SLA} has been applied and approach 3 for the near-wall function and Ψ is used. The choice of numerical scheme has a large impact on the mixing and the growth of the free shear layer. Without the low dispersion part of the numerical scheme, clear undepredictions of both the vorticity thickness and the momentum thickness are given as seen in Figure 14 (a)-(b). Peak values of resolved stresses are reasonably well captured at $x = 650$ mm as seen in Figures 14 (c) and 15 (a)-(c). However, the width of the stress profiles is too small for the simulations using the scalar dissipation scheme (SD) or the matrix dissipation scheme (MD) without the low dispersive part, which corresponds to the underpredicted mixing observed in the vorticity thickness and the momentum thickness.

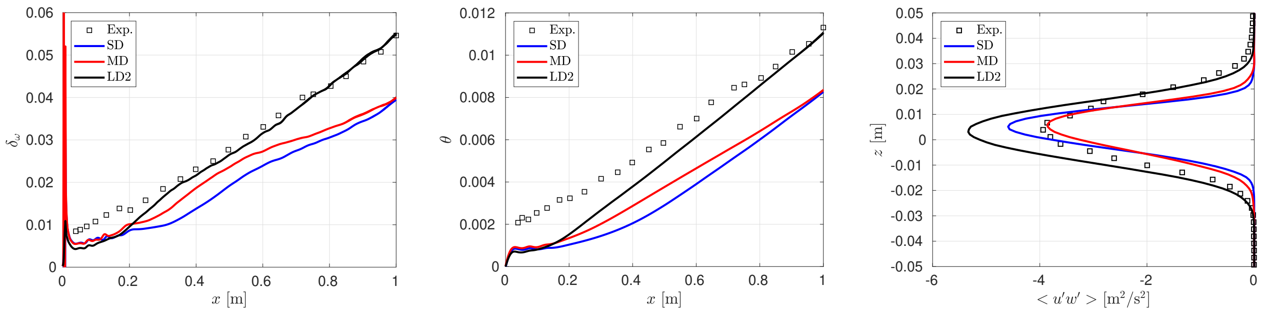

(a) Vorticity thickness. (b) Momentum thickness. (c) Resolved shear stress, $< u'w' >$.

Figure 14 – Free shear layer flow. Effect of numerical scheme, $\Delta = \Delta_{SLA}$. (a)-(b) Growth of vorticity thickness and momentum thickness. (c) Resolved shear stress, $< u'w' >$, at $x = 650$ mm.

4.3 Transonic cavity flow

The transonic flow over the generic M219 cavity has been simulated. Experimental data by Henshaw [24] and LES data by Lerchêveque et al. [25] are used for reference. The reference LES data used in this paper is from the simulation on the fine grid in [25]. The cavity has the dimensions (L, W, D)=$(5D;D;D)$, where D is the cavity depth, see Figure 16. Pressure fluctuations are sampled in the simulations at the same positions on the cavity floor as the Kulite transducers are located in the experiment. The x-positions of the Kulite transducers on the cavity floor are given in Table 3 and shown in Figure 16.

The reference LES simulations by [25] uses the same cavity dimensions as in the experiment, however, the geometry around the cavity is simplified. In the LES simulations the cavity is submerged in a flat plate and the wedge shaped wind tunnel setup shown in Figure 16 is not included.

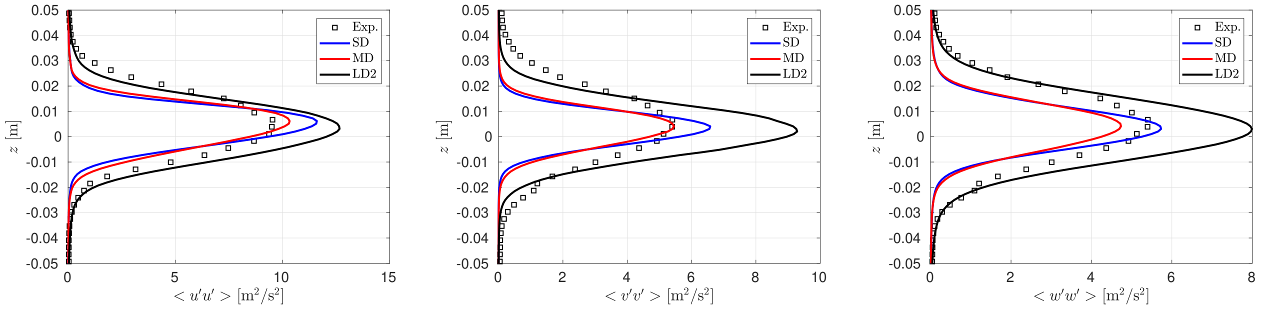

(a) $< u'u' >$. (b) $< v'v' >$. (c) $< w'w' >$.

Figure 15 – Free shear layer flow. Effect of numerical scheme, $\Delta = \Delta_{SLA}$. Resolved normal stresses at $x = 650$ mm.

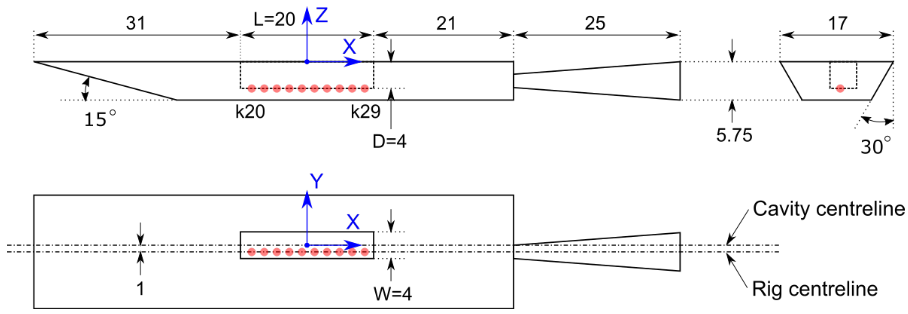

Figure 16 – Cavity flow. Schematics of the M219 cavity used in the wind tunnel test. The sting is excluded in the simulations. Measures in inch. Positions of Kulite transducers indicated by red markers, see also Table 3.

Table 3 – Positions of Kulite transducers on the cavity floor, $(y,z) = (-1.0, -4.0)$ inch.

	K20	K21	K22	K23	K24	K25	K26	K27	K28	K29
x [inch]	-9.0	-7.0	-5.0	-3.0	-1.0	1.0	3.0	5.0	7.0	9.0
x/D [-]	-2.25	-1.75	-1.25	-0.75	-0.25	0.25	0.75	1.25	1.75	2.25

The computational domain used in the simulations aims to mimic the wind tunnel setup, see Figure17. However, in the simulations we have chosen to exclude the wind tunnel sting in order to reduce the grid complexity and the number of grid points. The computational grid is shown in Figure 18.

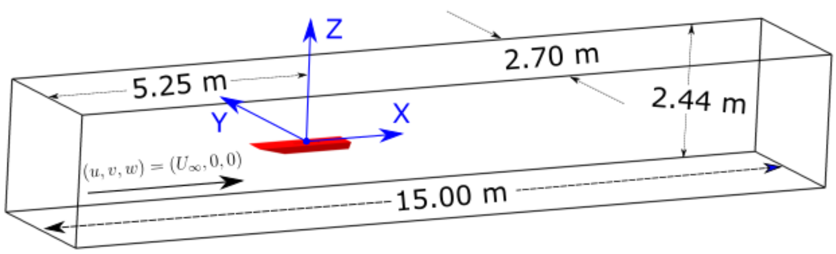

Figure 17 – Cavity flow. Computational domain. The domain size is similar to the wind tunnel test section.

The total number of hexahedral grid cells are approximately 70 millions. The largest grid cells inside the cavity are cube shaped with a side of maximum 2 mm. An H-grid topology has been used to keep grid lines orthogonal in order to minimize the impact of numerical discretization errors and errors in the turbulence modeling related to the grid.

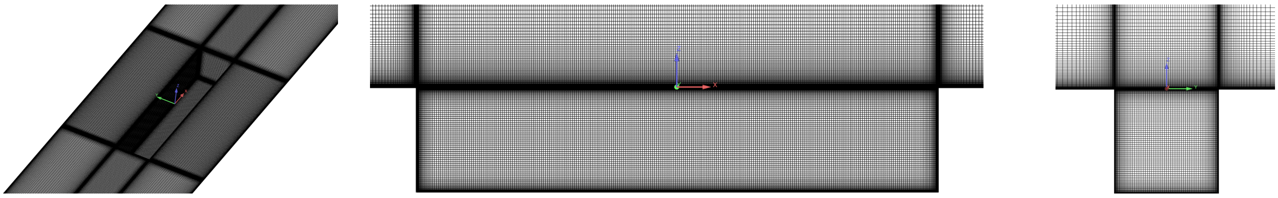

(a) Surface grid. (b) xz-plane, $y = 0$. (c) yz-plane, $x = 0$.

Figure 18 – Cavity flow. Computational grid.

The following freestream conditions have been used: $M_\infty = 0.85$, $P_{s,\infty} = 62100$ Pa and $T_{s,\infty} = 266.53$ K, which gives $(U_\infty, V_\infty, W_\infty) = (278.16, 0, 0)$ m/s. Wall functions are applied to all no-slip walls where the first grid point is located at $y^+ \approx 100$. The y^+-value is based on a SA-RANS simulation and it is evaluated in the boundary layer shortly upstream of the cavity leading edge. A time step of $\Delta t = 1 \cdot 10^{-5}$ s has been used. To establish the flow field 0.1 seconds were simulated and the statistical data used in the analysis is based on 0.5 seconds. In total 0.6 seconds have been simulated. For this test case $< \cdot >$ means averaging in time. The numerical schemes and modeling approaches used for this test case are summarized in Table 1.

We compare the mean flow field with the LES reference data [24] and the instantaneous flow field with the experimental data by [25]. For the instantaneous flow field we evaluate Sound Pressure Level (SPL) and Overall SPL (OASPL). From the SPL we identify the Rossiter modes. Sound pressure level and OASPL is calculated as follows

$$SPL = 10 \log_{10} \left(\frac{PSD}{p_{ref}^2} \right) \tag{13}$$

where $p_{ref} = 2.0 \times 10^{-5}$ Pa is the reference sound pressure and PSD is the power spectral density computed using Welch's method. A Hanning window is used and the signals from the CFD simulations are divided into 16 sections. The experimental data signal is much longer, approximately 3.4 seconds, and is divided into 64 segments. A window overlap of 50 per cent is used. The OASPL is calculated as

$$OASPL = 20 \log_{10} \left(\frac{p'_{rms}}{p_{ref}} \right) \tag{14}$$

where p'_{rms} is the root-mean-square value of the pressure fluctuation p', which is defined as the difference between the local instantaneous pressure and the local time-averaged pressure.

4.3.1 Mean flow field

Time-averaged streamwise and vertical velocity profiles as well as profiles for resolved shear stress and resolved turbulent kinetic energy at $y = 0$ are shown in Figure 19. The streamwise and vertical velocity profiles more or less coincide for all simulations except for the simulation where Δ_{max} has been used. A less filled streamwise velocity profile is obtained at $x/D = -2.5$ with Δ_{max} compared to the other simulations and the reference LES data. This difference is also seen further downstream of the cavity leading edge. For $z/D < 0$ Δ_{max} a clear positive vertical velocity is obtained, which is not seen in the other simulations.

It is observed that all simulations differ from the LES data when comparing the streamwise velocity profile at $x/D = -2.5$. However, the reader should take into account the fact that the LES reference data is from a simulation using a simplified geometry around the cavity. In the simulations presented in this paper we have used the wedge shaped wind tunnel configuration. The wedge shape of the cavity wind tunnel configuration results in a local angle of attack, which makes the flow to separate on the top plate of the cavity rig, see Figure 21. Hence, a difference between the velocity profiles at the leading edge of the cavity ($x/D = -2.5$) is to be expected, since the wedge shaped rig geometry is excluded in the LES reference simulation.

The SA-DDES simulations predict a much stronger negative vertical velocity compared to the reference LES data at $x/D = 2.5$. It is also observed that the SA-DDES simulations do not predict any negative vertical velocity for $x/D < 2.0$ in opposite to the LES reference simulation. However, the stronger negative vertical velocity predicted with SA-DDES at $x/D = 2.5$ is only a consequence of the positive vertical velocity upstream. The flow has to turn downwards (negative vertical velocity) due to the rear wall of the cavity. The later the flow turns, the higher the vertical velocity has to be to compensate for a smaller region of negative vertical flow.

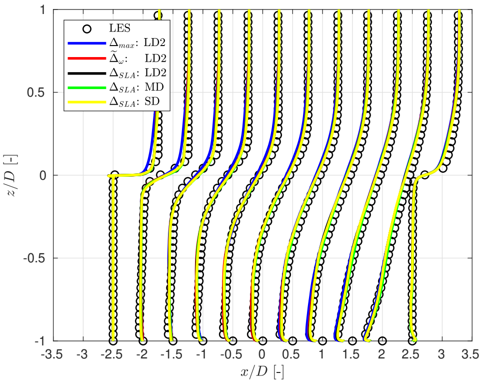

(a) Streamwise velocity, $< U >$.

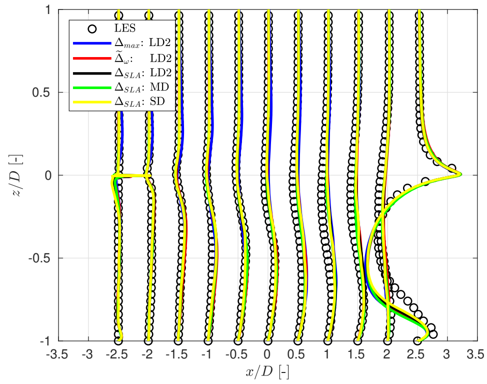

(b) Vertical velocity, $< W >$.

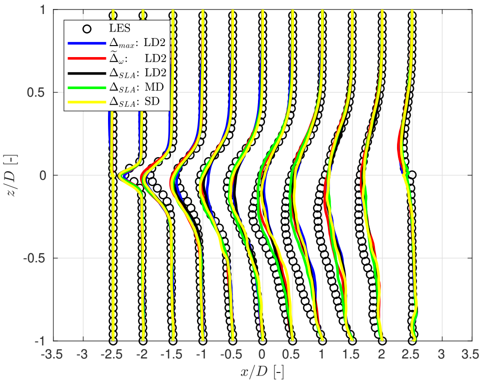

(c) Resolved shear stress, $< u'w' >$.

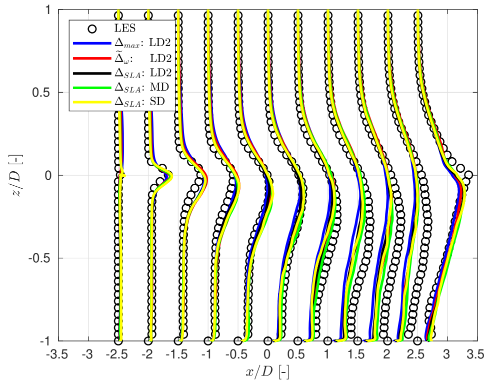

(d) Turbulent kinetic energy, k.

Figure 19 – Cavity flow. Profiles of (a) streamwise velocity, (b) vertical velocity, (c) resolved shear stress and (d) resolved turbulent kinetic energy.

The shear stress shown in Figure 19 (c) gives a good indication of the mixing and the growth of the free shear layer. The SA-DDES simulations compare reasonably well with the LES shear stress data for $x/D < 0$. For $x/D > 0$ the SA-DDES simulations predict a lower level of shear stress compared to LES data which is due to the fact that a less strong re-circulation is observed with SA-DDES. This is also reflected in the resolved turbulent kinetic energy presented in Figure 19, which is predicted lower with SA-DDES compared to the LES simulation.
The lowest level of resolved turbulence is obtained with Δ_{max} as seen in Figures 19 (c)-(d). This is explained by the high levels of turbulent viscosity given with this LES length scale, especially in the early stage of the free shear layer where the grid has high aspect ratio cells. Turbulent viscosity profiles are shown in Figure 20. The LES length scale $\widetilde{\Delta}_{\omega}$ reduces the turbulent viscosity compared to Δ_{max}, but Δ_{SLA} is also needed for this test case to rapidly reduce the turbulent viscosity.
In the early stage of the free shear layer, $x/D = -2.0$, Δ_{SLA} in combination with the LD2 scheme gives the largest peak value of resolved turbulence. It is however not evident that this combination is best suited for the flow further downstream and inside the cavity. The $\widetilde{\Delta}_{\omega}$ length scale performs somewhat better than Δ_{SLA} for $x/D \geq -0.5$ both regarding peak levels and the overall level of resolved turbulence.
The effect of the numerical discretization schemes evaluated is comparable with the effect of the different LES length scales. Moreover, it is not obvious from the mean flow field to declare that the LD2 scheme is superior over the MD and SD schemes, which it was shown to be in the fundamental free shear layer flow.

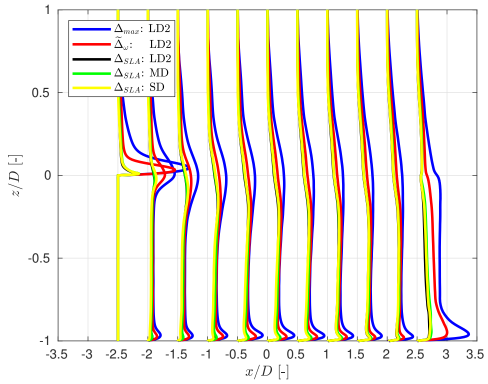

Figure 20 – Cavity flow. Profiles of turbulent viscosity.

4.3.2 Instantaneous flow field

Resolved turbulent structures are visualized using iso-surfaces of Q-criterion in Figure 21. It is also seen in this test case that the transition from RANS to turbulence-resolving LES flow is accelerated using the $\widetilde{\Delta}_{\omega}$ and Δ_{SLA} LES length scales compared to Δ_{max}. A much richer content of resolved turbulent structures are recognized with Δ_{SLA}.

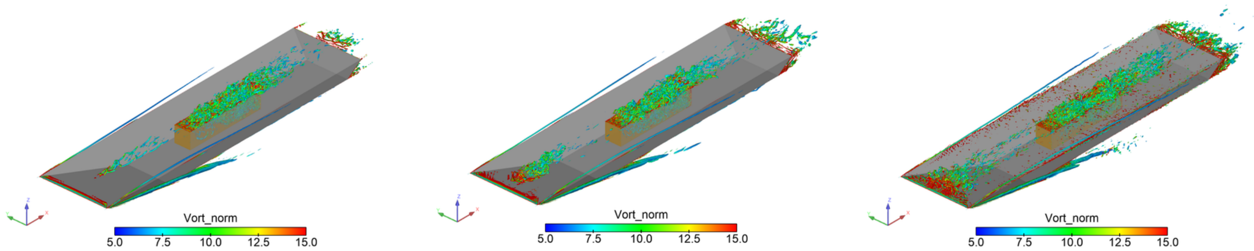

(a) $\Delta = \Delta_{max}$. (b) $\Delta = \widetilde{\Delta}_{\omega}$. (c) $\Delta = \Delta_{SLA}$.

Figure 21 – Cavity flow. Resolved turbulent structures visualized using iso-surfaces of Q-criterion, $Q\left(D/U_{free}\right)^2 = 10$. Colorbar shows scaled vorticity magnitude $\parallel \omega \parallel \left(D/U_{free}\right)$.

The choice of LES length scale has a large impact on the turbulent viscosity levels in the boundary layer on the rig top plate (not shown). As Δ_{SLA} resolves more turbulence in the flow separation bubble at the wedge shaped leading edge it also gives a substantially lower turbulent viscosity level compared to Δ_{max} and $\widetilde{\Delta}_{\omega}$ (not shown). Even though Δ_{max} is forced to be used in the calculation of the shielding function f_d for $f_d < f_{d0}$, with the aim to ensure sufficient shielding of the boundary layer (see Section 2), the very low levels of turbulent viscosity entering the f_d-function with Δ_{SLA} makes the model to switch from RANS to LES much closer to the wall compared to when Δ_{max} is used everywhere. Hence, with Δ_{SLA}, and to some extent also with $\widetilde{\Delta}_{\omega}$, resolved turbulence is present to a rather high degree inside the boundary layer at the cavity leading edge.

Rossiter modes identified from SPL are presented in Table 4. Sound pressure level for Kulite transducers K20-K29 as well as OASPL are shown in Figure 22. Overall, the best prediction of the Rossiter modes is made with Δ_{SLA} in combination with the LD2 scheme. The second mode is somewhat high in frequency with this combination both compared to the experimental data and the other simulations. The third mode is also predicted to be at a slightly higher frequency while the fourth mode is predicted at a somewhat lower frequency.

All simulations predict the first Rossiter mode reasonably well except for the simulation using $\widetilde{\Delta}_{\omega}$ with the LD2 scheme, which does not capture this mode at all. The second mode is predicted at a too high frequency in all simulations. So are the third and fourth modes. Only the simulation where Δ_{SLA} has been applied with the LD2 scheme, predict the fourth mode reasonably well. All other simulations, especially those not using the LD2 scheme predicts this mode at a much higher frequency compared to the experiment. It is worth to notice that with Δ_{max} in combination with the LD2 scheme the first two modes are predicted well in comparison to the experimental data.

Table 4 – Rossiter modes from SPL of cavity flow.

Mode	Exp. [24]	LES [25]	Δ_{max} (LD2)	$\widetilde{\Delta}_{\omega}$ (LD2)	Δ_{SLA} (LD2)	Δ_{SLA} (MD)	Δ_{SLA} (SD)
1	140	125	140	-	138	136	140
2	352	355	358	368	372	369	365
3	592	575	610	605	600	604	605
4	812	775	867	848	805	827	845

None of the simulations are able to capture the overall sound pressure level at all Kulite positions. With Δ_{SLA} and the LD2 scheme OASPL in K20-K23 are well predicted compared to the experimental data, but for transducers further downstream in the cavity too low levels of OASPL are predicted. With $\widetilde{\Delta}_{\omega}$ and the LD2 scheme, on the other hand, K25 to K29 are predicted in accordance to the experimental data. Using Δ_{SLA} with the MD scheme gives an OASPL similar to what is predicted with $\widetilde{\Delta}_{\omega}$ with LD2. Using Δ_{SLA} with the SD scheme gives a rather strong local decrease in OASPL at K24 which is not observed in the other simulations. With Δ_{max} and the LD2 scheme OASPL is predicted too low at all Kulite positions.

Adding together observations on the mean flow field with the analysis of instantaneous flow fields we come to the conclusion that Δ_{max} does not give satisfactory results for the used computational setup. Moreover, none of the length scales $\widetilde{\Delta}_{\omega}$ and Δ_{SLA} are superior over the other, even though they both perform better than Δ_{max}. The LD2 is favourable in the prediction of SPL, Rossiter modes and OASPL.

5. Summary and conclusion

The SA-DDES framework has been used to evaluate how the turbulence-resolving capability is affected by the choice of LES length scale and the numerical discretization scheme for the convective fluxes. Moreover, the impact on the turbulence-resolving capability due to the use of the near-wall functions in LES mode of SA-DDES has been evaluated. Decaying homogeneous isotropic turbulence, a low-speed fundamental free shear layer flow and the transonic flow over the generic M219 cavity have been simulated using the unstructured compressible flow solver M-Edge.

Three LES length scales have been evaluated; Δ_{max}, $\widetilde{\Delta}_{\omega}$ and Δ_{SLA}. The first length scale is used in the original formulation of SA-DDES and is based on the maximum length of the local control volume. The second length scale $\widetilde{\Delta}_{\omega}$ is based on the local vorticity field. The third length scale is based on $\widetilde{\Delta}_{\omega}$ but with an additional sensor to identify Kelvin-Helmholz like two-dimensional turbulent structures to further reduce the local turbulent viscosity in such regions in order to accelerate the development of turbulence-resolving LES flow.

It has been shown that the impact of the near wall functions (NWF) and the correction function Ψ are large for the SA model in LES mode. This has been demonstrated in decaying homogenous isotropic turbulence, where the correct decay of kinetic energy is only achieved when the near-wall functions and the Ψ-function are activated. However, in the case of free shear layer flow, the NWF and Ψ had a negative impact on the turbulent mixing and the development of LES resolved turbulent structures. In the fundamental free shear layer flow it was shown that the vorticity based LES length scales were needed to reasonably well capture the experimental growth of the mixing layer and the turbulent Reynolds stresses. Moreover, it was shown that the choice of numerical scheme has a large impact on the prediction of the mixing layer growth. A low-dissipative and low-dispersive (LD2) scheme was shown to give best results.

In the transonic cavity flow the free shear layer interacts with the flow re-circulation inside the cavity. The flow is characterized by strong pressure fluctuations and large-scale turbulence. For this flow the effect of the LES length scale and the numerical scheme was not as obvious as in the fundamental free shear layer. The use of Δ_{SLA} promotes the development of resolved turbulence in the early stages of the free shear layer also in this test case. However, for the re-circulating flow inside the cavity $\widetilde{\Delta}_{\omega}$ performs as good as Δ_{SLA}. For mean flow properties $\widetilde{\Delta}_{\omega}$ and Δ_{SLA} gave similar results. It was, however, observed that the choice of LES length scale has a large impact on the shielding of

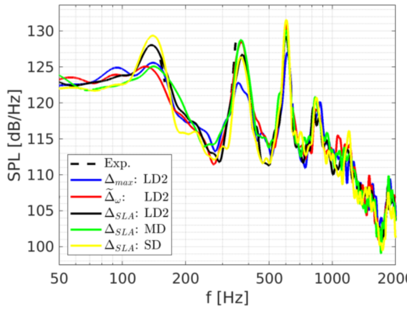

(a) SPL, K20.

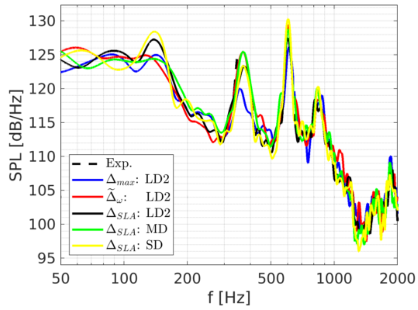

(b) SPL, K21.

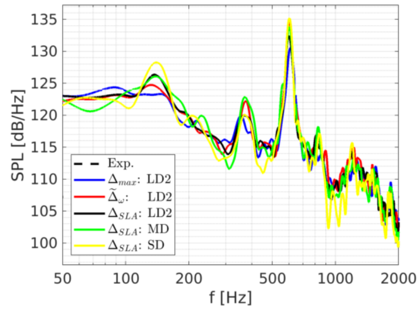

(c) SPL, K22.

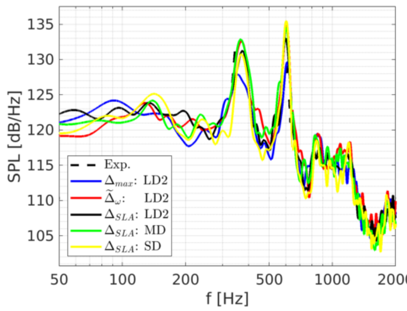

(d) SPL, K23.

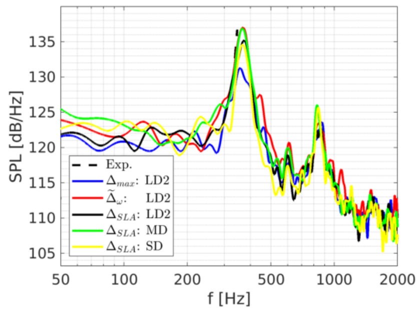

(e) SPL, K24.

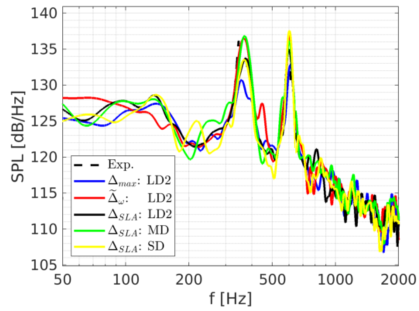

(f) SPL, K25.

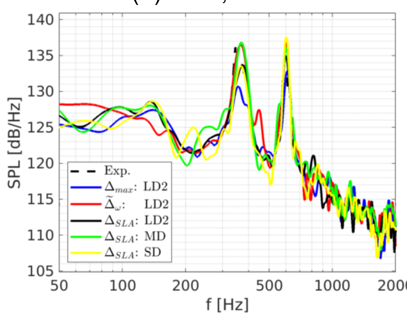

(g) SPL, K26.

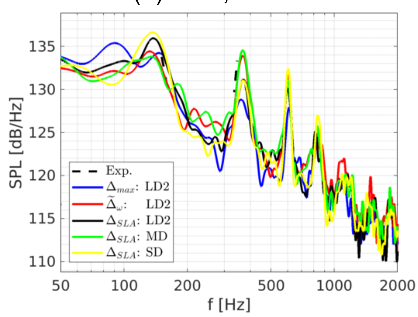

(h) SPL, K27.

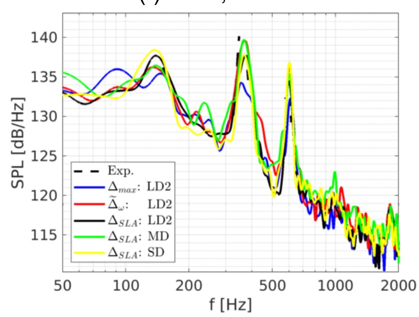

(i) SPL, K28.

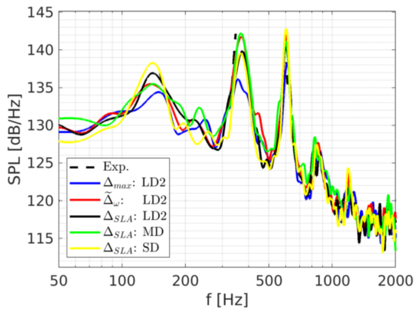

(j) SPL, K29.

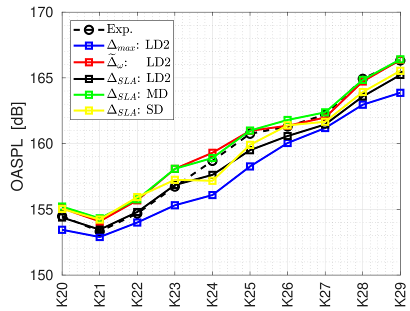

(k) OASPL, K20-K29.

Figure 22 – Cavity flow. (a)-(j) Sound pressure level (SPL). (k) Overall sound pressure level (OASPL).

the boundary layer for this case. A small separation at the leading edge of the wedge shaped wind tunnel rig makes SA-DDES to switch to turbulence-resolving mode with all three LES length scales. However, it was most evident with $\Delta = \Delta_{SLA}$, which gives a large portion of resolved turbulence in the boundary layer at the cavity leading edge indicating that the f_d-function needs to further investigated. The instantaneous flow field in the cavity was analyzed using sound pressure level (SPL) and overall SPL (OASPL) at the same positions as in the experiment. I was concluded that $\widetilde{\Delta}_\omega$ and Δ_{SLA} gives improved predictions of OASPL compared to Δ_{max}. The Rossiter modes were best predicted using the Δ_{SLA} length scale in combination the a low-dissipative and low-dispersive numerical scheme. However, the effect of the numerical scheme was observed to be much weaker for the cavity flow compared to the fundamental shear layer flow where the LD2 scheme was key to capture the experimental flow field. In this flow case the near-wall functions and Ψ were switch of in LES mode.

Acknowledgment

This work has been funded by the Swedish Governmental Agency for Innovation Systems (VINNOVA), the Swedish Defence Materiel Administration (FMV) and the Swedish Armed Forces within the National Aviation Research Programme (NFFP, Contract Numbers 2017–04887 and 2019-02779) and Saab Aeronautics.

Contact Author Email Address

sebastian.arvidson@saabgroup.com or sebastian.arvidson@chalmers.se

Copyright Statement

References

[1] P. Spalart, W-H. Jou, M. Strelets, and S.R. Allmaras. Comments on the feasability of les for wings, and on a hybrid rans/les approach. In *Advances in DNS/LES*, pages 137–147, Ruston, Lousiana, 1997.

[2] P.R. Spalart, S. Deck, M.L. Shur, K.D. Squires, M. Kh. Strelets, and A. Travin. A new version of detached-eddy simulation, resistant to ambiguous grid densities. *Theory of Computational Fluid Dynamics*, 20:181–195, 2006.

[3] M.L. Shur, P.R. Spalart, M.Kh. Strelets, and A.K. Travin. A hybrid RANS-LES approach with delayed-DES and wall-modelled LES capabilities. *International Journal of Heat and Fluid Flow*, 29:1638–1649, 2008.

[4] S. Deck. Zonal-Detached-Eddy Simualtion of the Flow Around a High-Lift Configuration. *AIAA Journal*, 43:2372–2384, 2005.

[5] S. Deck. Recent improvments in the zonal detached eddy simualtion (ZDES) formulation. *Theoretical and Computational Fluid Dynamics*, 2012.

[6] S. Deck and N. Renard. Towards an enhanced protection of attached boundary layers in hybrid rans/les methods. *Journal of Computational Physics*, 400:108970, 2020.

[7] C. Mockett, W. Haase, and F. Thiele. Go4hybrid: A European Initiative for Improved Hybrid RANS-LES Modelling. In S. Girimaji, W. Haase, S-H. Peng, and D. Schwamborn, editors, *Progress in Hybrid RANS-LES Modelling*, volume 130 of *NNFM*, pages 299–303, Cham, 2015. Springer International Publishing.

[8] N. Chauvet, S. Deck, and L. Jaquin. Zonal Detached Eddy Simualtion of a Controlled Propulsive Jet. *AIAA Journal*, 45:2458–2473, 2007.

[9] M. L. Shur, P. R. Spalart, M Kh. Strelets, and A. K. Travin. An enhanced version of des with rapid transition from rans to les in separated flows. *Flow, Turbulence and Combustion*, 95(4):709–737, 2015.

[10] P.R. Spalart and S.R. Allmaras. A one-equation turbulence model for aerodynamic flows. *La Recherche Aérospatiale, 1, p. 5-21*, 1:5–21, 1994.

[11] C. Mockett. *A comprehensive study of detached-eddy simulation*. PhD thesis, der Technischen Universität Berlin, 2009.

[12] S. Arvidson, L. Davidson, and S.-H. Peng. Hybrid RANS-LES Modeling Using a Low-Reynolds-Number $k-\omega$ Based Model. AIAA paper 2014-0225, National Harbour, Maryland, 2014.

[13] C. Mockett, M. Fuchs, A. Garbaruk, M. Shur, P. Spalart, M. Strelets, F. Thiele, and A. Travin. Two Non-zonal Approaches to Accelerate RANS to LES Transition of Free Shear Layers in DES. In S. Girimaji, W. Haase, S-H. Peng, and D. Schwamborn, editors, *Progress in Hybrid RANS-LES Modelling*, volume 130 of *NNFM*, pages 187–201, Cham, 2015. Springer International Publishing.

[14] P. Eliasson. Edge, a navier–stokes solver for unstructured grids. *Finite Volumes for Complex Applications*, 3:527–534, 2002.

[15] P. Eliasson and P. Weinerfelt. Recent applications of the flow solver edge. 7th Asian CFD Conference, 2007.

[16] P. Eliasson, P. Weinerfelt, and F. Bramkamp. Enhancing CFD predictions of the Gripen aircraft. International Council of Aeronautical Sciences, 2022.

[17] P. Eliasson, S. Eriksson, and J. Nordström. The influecne of weak and strong solid wall boundary conditions on the convergence to steady-state of the Navier-Stokes equations. AIAA paper, No. 2009-3551, 2009.

[18] J. Löwe, A. Probst, T. Knopp, and R. Kessler. Low-dissipation low-dispersion second-order scheme for unstructured finite-volume flow solvers,. *AIAA Journal*, 54, 2016.

[19] R.C Swanson and Eli Turkel. On central-difference and upwind schemes. *Journal of Computational Physics*, 101(2):292–306, 1992.

[20] S. Langer. Investigations of a compressible second order finite volume code towards the incompressible limit. *Computers & Fluids*, 149:119–137, 2017.

[21] M. Carlsson, L. Davidson, S.-H. Peng, and S. Arvidson. Parametric Investigation of Low-dissipation Low-dispersion Schemes for Unstructured Flow Solvers in Large Eddy Simulation. AIAA SciTech 2020 paper, 2020.

[22] G. Comte-Bellot and S. Corrsin. Simple Eularian time correlation of full- and narrow-band velocity signals in grid-generated isotropic turbulence. *Journal of Fluid Mechanics*, 48(2):273–337, 1971.

[23] J. Delville. *La décomposition orthogonale aux valeurs propres et l'analyse de l'organisation tridimensionnelle des écoulements turbulents ci saillés libres*. PhD thesis, Université de Poitiers, 1995.

[24] MJ de C. Henshaw. M219 cavity case, verification and validation data for computational unsteady aerodynamics. Technical report , Military Aircraft and Aerostructures, Brittish Aerospace (Operations) Ltd, 1991.

[25] L. Larchêque, P. Sagaut, T.-H. Lê, and P. Comte. Large-eddy simulation of a compressible flow in a three-dimensional open cavity at high Reynolds number. *Journal of Fluid Mechanics*, 516:265–301, 2004.